





# Si<sub>2</sub>Te<sub>3</sub> Photodetectors for Optoelectronic Integration at Telecommunication Wavelengths

Srinivasa Reddy Tamalampudi , Ghada Dushaq , Juan E. Villegas , *Student Member, IEEE*, Bruna Paredes ,  
and Mahmoud S. Rasras, *Senior Member, IEEE*

**Abstract**—High-performance two-dimensional (2D) - photodetectors with the potential for on-chip integration are desired for telecommunication applications. This work presents the photoreponse of planar silicon telluride photodetector (Si<sub>2</sub>Te<sub>3</sub>) with under wavelengths of 1310 and 1550 nm light illuminations. We utilized mechanically exfoliated multilayered Si<sub>2</sub>Te<sub>3</sub> to fabricate back-gated phototransistor. The device with  $\sim 50$  nm Si<sub>2</sub>Te<sub>3</sub> flake thickness demonstrated a hole mobility of  $0.36 \text{ cm}^2 \text{ V}^{-1} \text{ s}^{-1}$  and photo-responsivities of  $170.5 \text{ AW}^{-1}$  ( $0.35 \text{ } \mu\text{W}$ ), and  $12.1 \text{ AW}^{-1}$  ( $0.25 \text{ } \mu\text{W}$ ) at 1310 nm and 1550 nm excitations, respectively. Furthermore, the frequency response of the device with two different metal contacts (Au/Cr and Al/Ti) was tested. The device exhibited moderate broadband response with Au/Cr metal contact of 3dB bandwidth of 1.6 MHz, while 3.8 MHz bandwidth is realized with Al/Ti metal contacts. We also demonstrated a prototype of a heterogeneously integrated Si<sub>2</sub>Te<sub>3</sub> photodetector onto a Si waveguide. The transmission losses in the waveguide were measured before and after the integration. Results demonstrated an attenuation of the optical signal by 24.3 dB and 18 dB for 1310 nm and 1550 nm wavelengths, respectively, that can attribute to the material induced losses. These findings suggest that Si<sub>2</sub>Te<sub>3</sub> is a promising 2D semiconductor material for optical communication photodetection.

**Index Terms**—2D materials, photodetectors, telecommunication wavelengths, Si-on-chip integrated.

## I. INTRODUCTION

SILICON photonics is a standard technology for next-generation on-chip optoelectronic applications [1]. Mainstream and long-distance data transmission employ 1300–1550 nm laser wavelengths given the minimum optical losses for silica optical fibers in this spectrum [1]. Therefore, the development of new photodetectors operating at this bandwidth is actively pursued. The direct growth of germanium and III–V group materials on a silicon (Si) substrate is technologically challenging due to the mismatch of lattice constants and thermal expansion coefficients [2].

Manuscript received July 31, 2021; revised September 25, 2021; accepted November 4, 2021. Date of publication November 9, 2021; date of current version December 15, 2021. This work was supported by NYUAD Research Enhancement Fund. (*Corresponding authors: Srinivasa Reddy Tamalampudi.*)

The authors are with the Department of Electrical and Computer Engineering, New York University of Abu Dhabi, Abu Dhabi, Saadiyat Marina 129188, United Arab Emirates (e-mail: st4212@nyu.edu; ghd1@nyu.edu; jev1@nyu.edu; bp64@nyu.edu; mr5098@nyu.edu).

This article has supplementary material provided by the authors and color versions of one or more figures available at <https://doi.org/10.1109/JSTQE.2021.3126612>.

Digital Object Identifier 10.1109/JSTQE.2021.3126612

To overcome these limitations, the use of layered 2D materials shows great potential. Layered 2D materials provide a wide range of inimitable properties such as high mechanical flexibility and van der Waal forces between the layers, making them ideal for heterogeneous integration for on-chip interconnects[3]. For this, only a few 2D semiconductor systems have been verified with telecom wavelengths photodetection capability including graphene, [4] black phosphorus,[5] PtSe<sub>2</sub>, [6] GeP, [7], [8] Tellurium, [9] MoTe<sub>2</sub> [10]; Several recent studies demonstrate the integration of graphene onto Si photonic chips for various applications such as modulators and photodetectors [11]–[13]. Recently, a plasmonically enhanced waveguide-integrated graphene photodetector exhibited ultrahigh bandwidth of 110 GHz with an external responsivity of  $\sim 0.5 \text{ A W}^{-1}$  at telecom wavelengths [14]. While another study reported a graphene photodetector with polymeric gate dielectric on a passive optical waveguides demonstrated a bandwidth of 67 GHz with zero dark current [15]. Although a promising progress has been made in the context of these applications, graphene suffers from low photoresponsivity. Subsequently, waveguide integrated black phosphorus (BP) photodetectors were widely studied for telecom applications. Devices exhibited a 3 GHz bandwidth [16]. However, its highly unstable nature at ambient conditions hampers its applications. Recently, on-chip integrated strained MoTe<sub>2</sub> TMDC (transmission metal dichalcogenide) photodetectors gained attention where a bandwidth of 35 MHz is reported [17]. Despite its excellent opto-electronic properties, most TMDC materials are still limited in their response to the visible spectrum (above the Si band gaps) [18]. This has hindered their wide deployment in telecommunications applications. Nonetheless, novel 2D materials, especially those sensitive to telecom wavelength bands, are still to be explored.

Recently, Si-based layered 2D silicon telluride (Si<sub>2</sub>Te<sub>3</sub>) is gaining a lot of attention by its potential applications ranging from thermoelectric to optoelectronic devices and chemical sensors [19]–[23]. Si<sub>2</sub>Te<sub>3</sub> is a red, transparent, p-type layered semiconductor with an indirect bandgap of 1.1 eV and a direct bandgap of 2.2 eV [24]. Recent studies on Si<sub>2</sub>Te<sub>3</sub> indicate anisotropic optoelectronic properties and a bandgap tunability that depends on the orientations of the Si-Si dumbbells and the stoichiometry of the crystal, [24], [25] as well as the capacity for its direct growth on various substrates through different mechanisms, [21], [25]–[27] indicating its potential use in future opto-electronics. Additionally, Si<sub>2</sub>Te<sub>3</sub> has intrinsic crystal defects (recombination centers and trap states), which governs

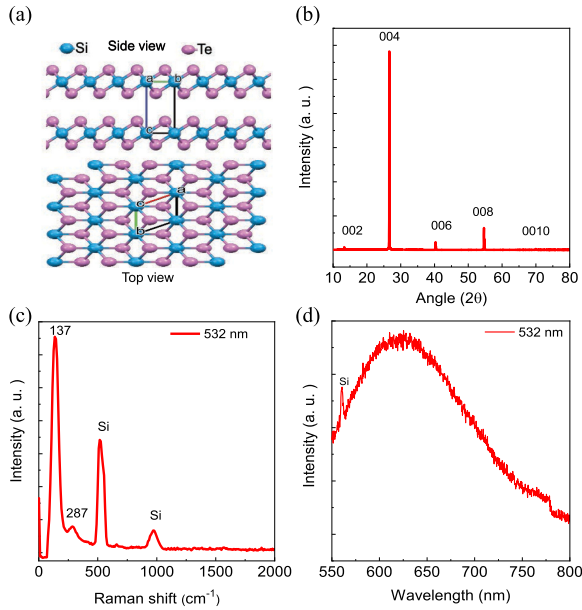


Fig. 1. (a) Schematic illustrations of the Si<sub>2</sub>Te<sub>3</sub> crystal, side, and top views. (b) XRD spectrum of single crystal Si<sub>2</sub>Te<sub>3</sub>. (c) Raman spectrum of the exfoliated multi-layered Si<sub>2</sub>Te<sub>3</sub> flake under 532 nm excitation. (d) Photoluminescence spectrum of the Si<sub>2</sub>Te<sub>3</sub>.

the absorption of the crystal from visible to infrared regions (2.2 eV to 0.45 eV). Moreover, it is important to note that the change in the stoichiometry in the direction of excess tellurium greatly influences the spectral distribution of the photoconductivity of the Si<sub>2</sub>Te<sub>3</sub> crystals [22]. However, the reported responsivity is limited to 404–1050 nm, which is analogous to the higher wavelength absorption limit of silicon based photodetectors [28]. In-depth studies on the performance of the Si<sub>2</sub>Te<sub>3</sub> devices for telecommunication bands around 1310 nm and 1550 nm are still missing. Here, to the best of our knowledge, we report for the first time a stable Si<sub>2</sub>Te<sub>3</sub> photodetector in operating in the telecom wavelengths. Additionally, we verify the ability to transfer a Si<sub>2</sub>Te<sub>3</sub> flake onto a Si photonic chip on top of a waveguide using the dry 2D material transfer method and we investigated the Si<sub>2</sub>Te<sub>3</sub> integrated waveguide optical losses in C (1535–1565 nm) and O (1260–1360) bands and waveguide integrated photodetector performance. In Section II, the experimental results are discussed including material characterization and device fabrication. Then, optical testing, responsivity and dynamic response of the device are presented. The integration on silicon waveguide is shown in subsection Section II.E of the experimental results. Finally, the conclusions are given in Section III.

## II. EXPERIMENTS AND RESULTS

### A. Material Characterization

Figure 1(a) upper and bottom panels shows schematic representations of the side and top views of the Si<sub>2</sub>Te<sub>3</sub> crystal respectively. The crystal structure features hexagonal closest packed layers of Te atoms with disordered [Si<sub>2</sub>] dumbbells residing in 2/3 of all octahedral voids of every second layer enclosed by Te

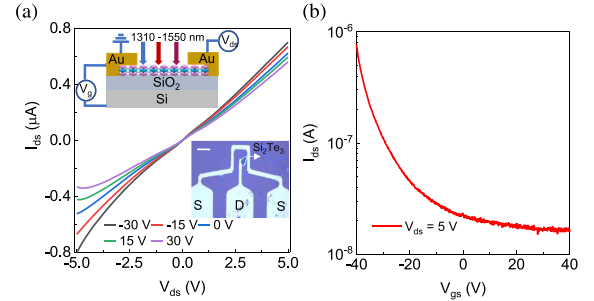


Fig. 2. (a) Output characteristic curves obtained for V<sub>gs</sub> values from -30 to 30 V. The top and bottom insets show a schematic illustration of a multi-layered Si<sub>2</sub>Te<sub>3</sub> back-gated FET and Optical microscopy image of the fabricated device respectively. The scale bar is 20 μm. (b) The transfer curve of the FET was measured by scanning V<sub>gs</sub> from -40 V to 40 V at V<sub>ds</sub> = 5 V on a logarithmic scale.

atoms.[29] To determine the crystal properties, first, we analyzed the X-ray diffraction (XRD) of the 2D semiconductors crystal. As shown in Fig. 1b, the obtained XRD peaks are similar to the ones reported for Si<sub>2</sub>Te<sub>3</sub> and the sharp peaks demonstrated a single crystal nature [30]. Energy dispersive X-ray spectroscopy (EDX) elemental mapping was used to determine the elemental composition and verify the distribution of the elements (Si and Te) throughout the entire sample. Figure S1a shows a scanning electron microscopy image (SEM) of the crystal. The corresponding elemental spectrum and uniform mapping distribution of the elements are shown in Fig. S1(b-d).

Furthermore, Micro-Raman spectroscopy and photoluminescence measurements with 532-nm laser excitation were performed to determine the phonon modes and the broad emission peak of the bulk Si<sub>2</sub>Te<sub>3</sub> crystal. As shown in Fig. 1c, the phonon mode peak at A<sub>g</sub> (137 cm<sup>-1</sup>) corresponds to the out-of-plane vibration from the Te atoms, while the one at E<sub>g</sub> (287 cm<sup>-1</sup>) corresponds to the in-plane vibration of Si atoms [20], [21], [31]. Irrespective of the growth method, Si<sub>2</sub>Te<sub>3</sub> typically possesses a large defect density of up to 10<sup>17</sup> cm<sup>-3</sup>, which contributes to a broad photoluminescence emission in the region of the visible to the near-infrared region (see Fig. 1d) [24], [32]. The measured XRD, EDX, Raman and photoluminescence measurements are consistent with previous reported studies on Si<sub>2</sub>Te<sub>3</sub> crystals.

### B. Device Fabrication and Electrical Measurement

We investigated the electrical properties of 50 nm multi-layered Si<sub>2</sub>Te<sub>3</sub> flake using a back-gated FET configuration. An atomic force microscope (AFM) topography and height profile are shown in the Fig. S2, confirmed the thickness of the flake. The layered thickness is selected to maximize the absorption, given that recently, it has been reported that the 550 nm to 1050 nm broadband Si<sub>2</sub>Te<sub>3</sub> photoluminescence decreases drastically for 20 nm thick flakes, and completely disappears for sub 9 nm thickness [33]. A schematic of the device is shown in the top inset of Fig. 2a. To fabricate the FET, mechanically exfoliated Si<sub>2</sub>Te<sub>3</sub> crystal flakes (2d semiconductor, Inc.) were transferred onto a 285 nm thick SiO<sub>2</sub> substrate. Metal electrodes of chromium (Cr) / gold (Au) (15/90 nm) were fabricated through lift-off using UV photo-lithography and E-Beam evaporation. An optical image of

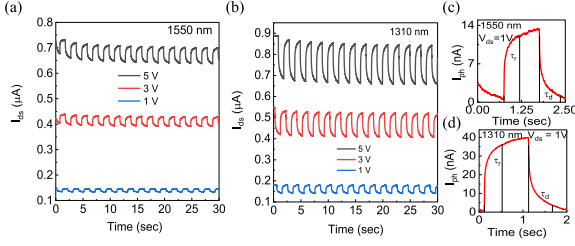


Fig. 3. Temporal response of the Si<sub>2</sub>Te<sub>3</sub> photodetector. (a-b) The measured cyclic response under pulsed illuminations for  $\lambda = 1550$  nm and 1310 nm for different bias voltages ( $V_{ds} = 1$  V, 3 V, and 5 V). (c-d) The measured rise and decay times of the photodetector for  $\lambda = 1550$  nm and 1310 nm, respectively at  $V_{ds} = 1$  V.

a lateral fabricated photodetector is depicted in bottom inset of Fig. 2a. An Agilent B1505A curve tracer/power device analyzer was used to measure the I-V characteristics of the fabricated devices at various back gate voltages ( $V_{gs}$  from -30 to 30 V), as shown in Fig. 2a. The curves exhibit a linear behavior indicating a good ohmic contact between the deposited Cr/Au electrodes and the Si<sub>2</sub>Te<sub>3</sub> channel. Furthermore, the devices were electrically characterized by applying a constant drain-source voltage ( $V_{ds}$ ) while sweeping the back-gate voltage  $V_{gs}$ . The plots of the transfer characteristics ( $I_{ds}$  vs  $V_{gs}$ ) between -40 to +40 V at  $V_{ds} = 5$  V are shown in Fig. 2b. From these plots, it is observed that the multi-layered Si<sub>2</sub>Te<sub>3</sub> channels exhibited a p-type semi-conductive behavior which can be attributed to the generation of Si vacancies during the crystal growth [29].

The effective field-effect hole mobility ( $\mu_h$ ) of the multi-layered Si<sub>2</sub>Te<sub>3</sub>-FET is obtained from the  $I_{ds}$ - $V_{gs}$  curve in the linear regime. It can be estimated from the equation  $\mu_h = (L/WC_{ox}V_{ds}) (\frac{\Delta I_{ds}}{\Delta V_g})$ , where  $C_{ox} = \epsilon_{ox}/t_{ox}$  is the capacitance per unit area. Here,  $\epsilon_{ox}$  is the permittivity of the gate dielectric and  $t_{ox}$  is the thickness of the insulating SiO<sub>2</sub> layer. We use an estimated channel length  $L = 12$   $\mu$ m and width  $W = 13$   $\mu$ m, resulting in a hole mobility of  $\sim 0.36$  cm<sup>2</sup> V<sup>-1</sup> s<sup>-1</sup>. This value is similar to the previously demonstrated ones for 2D MoS<sub>2</sub> and InSe [34], [35].

### C. Optical Measurements

To verify the response of the Si<sub>2</sub>Te<sub>3</sub> for 1550 nm and 1310 nm wavelengths, we conducted transient photocurrent studies. Shown in Figs. 3(a)-(b) is the generated channel current in a multi-layered Si<sub>2</sub>Te<sub>3</sub> FET at different bias voltages and 0 V gate bias, clearly demonstrating that it responds to the light switching. The temporal photo response was measured using an on/off cycle of 2 s. The test was performed for 100 secs and a good return to the original dark current level was observed, showing good reliability and reversibility of Si<sub>2</sub>Te<sub>3</sub> photodetector (see Fig. S3). The resulting photocurrents ( $I_{ph} = I_{light} - I_{dark}$ ) derived from Fig. 3(a)-(b) by subtracting the corresponding dark current from each dataset, plotted in Fig. S4, showed that the photocurrent increases with increasing bias voltage.

The dynamic response of the photocurrent can be expressed as  $I(t) = I_0 (1 - \exp(-t/\tau_r))$  and  $I(t) = I_0 \exp(-t/\tau_d)$  where

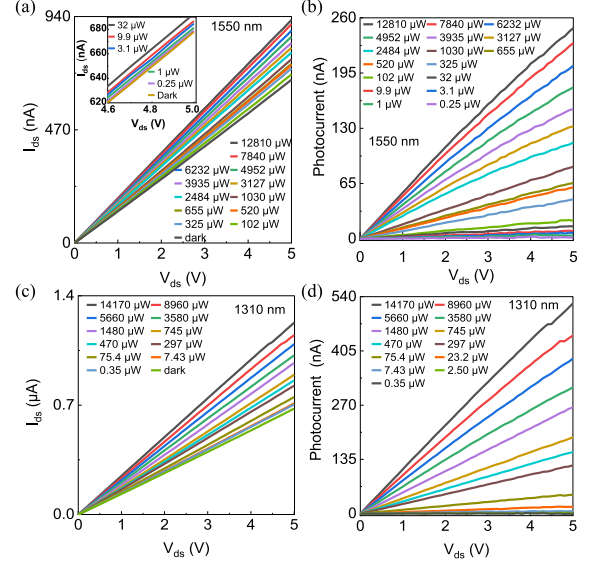


Fig. 4. Optoelectronic characterization of a multi-layered Si<sub>2</sub>Te<sub>3</sub> photodetector. (a) Typical output curves ( $I_{ds}$ - $V_{ds}$ ) of a multi-layered Si<sub>2</sub>Te<sub>3</sub> photodetector acquired in the dark and with 1550 nm illumination at various excitation laser powers while sweeping the  $V_{ds}$  bias voltage from 0V to 5V. Figure a inset shows the curves under dark and up to 32  $\mu$ W power illumination. (b) The measured photocurrent under 1550 nm laser excitations at different laser powers. (c-d)  $I_{ds}$ - $V_{ds}$  and photocurrent measurements under 1310 nm excitation respectively.

$\tau_r$  and  $\tau_d$  are the rise and decay time constants, respectively. Here the rise (decay) time is defined as the time that it takes for the current to increase (decrease) from 10% (90%) of the saturation value to 90% (10%).

The higher bias voltage accelerates the carriers drift and sweeps them out of the channel to contribute to a higher photocurrent. It was observed that the generated photocurrent under 1550 nm and 1310 nm excitations were different, which can be attributed to average penetration depths of excitation light into the photodetector which is determined by the wavelength-dependent absorption coefficient. Next, we retrieved the response time of the detector by using a single cyclic test as show in Fig. 3(c)-(d). Under 1550 nm (1310 nm) excitation, the measured rise ( $\tau_r$ ) and decay times ( $\tau_d$ ) were 0.45s (0.41 s) and 0.57 s (0.54 s), respectively. The measured  $\tau_r$  and  $\tau_d$  values are similar to recently reported Si<sub>2</sub>Te<sub>3</sub> photodetector response values [28]. It is worth mention that these measurements were limited to our Agilent system resolution of 0.1ms.

Next, we evaluated the behavior of the detector under different laser powers. The samples were top illuminated using a single-mode pigtailed GRIN fiber collimator (Thorlabs). The dependence of the output ( $I_{ds}$ - $V_{ds}$ ) curves on the incident optical power at 1550 nm wavelength is shown in Fig. 4a. The curves are measured under dark and illumination conditions with output laser power ranging from 0.25  $\mu$ W to 12810  $\mu$ W. For better visibility,  $I_{ds}$ - $V_{ds}$  curves under dark to 32  $\mu$ W were plotted in the inset of Fig. 4a. We observed an increase in the photo current as the excitation laser power increases. As expected, the photogenerated electron and hole pairs are swept to the metal electrodes in the opposite directions guided by the drain-source electric field, resulting in a channel current. The

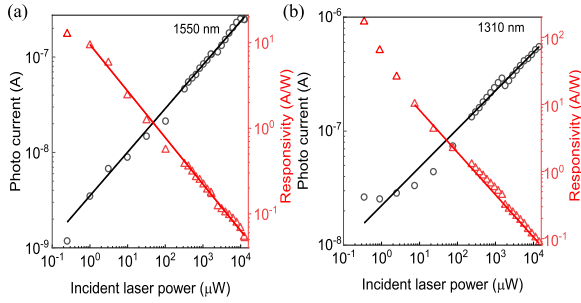


Fig. 5. Photocurrent (black open circles) and responsivity (red open triangles) as a function of illumination intensity at  $V_{ds} = 5$  V and  $V_g = 0$  V at 1550 and 1310 nm, respectively, and fitted power law.

corresponding incident laser power dependent photocurrents are depicted in Fig. 4b. Similarly, the output curves and photocurrent of the device measured under 1310 nm excitation are shown in Fig. 4(c)-(d) for incident optical powers in the range of from 0.35  $\mu$ W to 14170  $\mu$ W.

One critical figure-of-merit that determines the performance of a photodetector is the responsivity defined as the ratio of the generated photocurrent ( $I_{ph}$ ) to the incident optical power density ( $P$ ) on a detector area ( $S$ ). It is given by  $R = I_{ph}/P \cdot S$ . As shown in Fig. 5a, we measured responsivity of  $\sim 12.1$  AW<sup>-1</sup> under the illumination of 1550 nm at the illumination laser power of 0.25  $\mu$ W ( $I_{ph} = 1.18$  nA,  $P = 0.024$  mW/cm<sup>2</sup>,  $S = 365$   $\mu$ m<sup>2</sup>, radius of the incident spot size is 565  $\mu$ m<sup>2</sup>). We observed a sublinear increase in photocurrent and decrease in responsivity following the power laws of photocurrent ( $I_{ph}$ )  $\propto P^{0.45}$  and responsivity ( $R$ )  $\propto P^{-0.54}$  respectively. We also obtained similar results at 1310 nm excitation, see Fig. 5b. The responsivity reaches 170.5 AW<sup>-1</sup> under illumination at 1310 nm at a laser power of 0.35  $\mu$ W. The power laws of  $I_{ph} \propto P^{0.33}$  and  $R \propto P^{-0.61}$  were determined from fitting the measured data. It is important to note that, under both wavelength excitations, the responsivity drops as the laser power increases which can be attributed to Pauli blocking or trap states [36].

This result suggests that the photocurrent flowing through the device does not proportionately increase as the incident light intensity increases. The logarithmic plots of photocurrents in Figs. 5a and 5b show sublinear characteristics that indicate the existence of trap states. Our fabricated Si<sub>2</sub>Te<sub>3</sub> devices with an intrinsic defect show an ohmic behavior with the Au/Cr contacts, thus allowing the photo-gain mechanism. This mechanism in 2D materials arises due to defects and trap states in the photodetector channel. Under laser excitation, the minority carriers (electrons) are trapped and the majority carriers (holes) have a faster transit time ( $\tau_t$ ) across the device's channel which enhances the lifetime of the minority carriers ( $\tau_l$ ).

Due to the external bias voltage, the majority carriers reach the metal contact and exit the device while new ones get injected from the opposite contact which maintains charge neutrality. The injected majority carriers travel in the channel until they recombine with minority carriers. This process enhances the photo-generated current per incident photon and yields a higher photocurrent. The electrostatic field set up by the trapped charges tends to spatially separate the photogenerated electron-hole pair

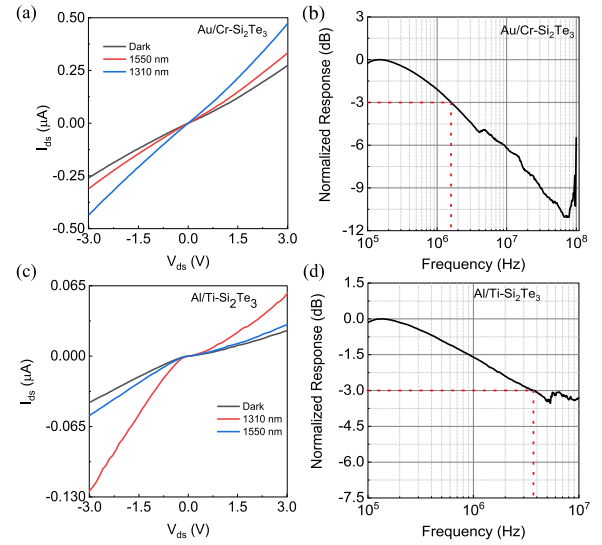


Fig. 6. Dynamic response of Si<sub>2</sub>Te<sub>3</sub> photodetector. (a)  $I_{ds}$ - $V_{ds}$  curves of Si<sub>2</sub>Te<sub>3</sub> photodetector under dark and telecom wavelength excitations with Au/Cr metal contacts. (b) The frequency response of the device with Au/Cr contacts. (c)-(d)  $I_{ds}$ - $V_{ds}$  curves and the frequency response of the Si<sub>2</sub>Te<sub>3</sub> device with Al/Ti contacts respectively.

[36]. Under low light intensities, the deep-lying, long-lived electron traps fill first. As we increase the laser intensity, the deep-trap states get saturated and the short-lived shallow electron traps populate and dominate the charge recombination dynamics. Due to existence of traps, the photogenerated carrier and photocurrent do not increase accordingly, which results in a decrease in the responsivity as exhibited in Figs. 5(a)-(b). Similar phenomena were previously reported for MoS<sub>2</sub> and InSe based photodetectors [34], [35].

#### D. Si<sub>2</sub>Te<sub>3</sub> Dynamic Response

Next, the photodetector frequency response was investigated. For this purpose, the Si<sub>2</sub>Te<sub>3</sub> device with Au/Cr metal contacts is irradiated by an amplified modulated 1310 nm continuous-wave laser. The laser is modulated by a commercial optical modulator (MOD) driven by a reference signal from a lock-in amplifier. A bias voltage was applied through RF probe using a bias-T and transimpedance amplifier. The schematic of the measurement setup was shown in Fig. S4. The photodetector with Au/Cr contacts showed an ohmic nature as depicted in the Fig. 6a. The device exhibited a moderate broadband frequency response of 3dB bandwidth of 1.6 MHz at 12 V with an incident power 6.4 W/cm<sup>2</sup> (See Fig. 6b). However, it is known that the bandwidth of the photodetectors depends on many parameters such as contact type (Schottky/ohmic), the thickness of the photodetector, device configuration (horizontal/vertical device), applied bias voltage, and spacing between the electrodes. In this study, we further investigate the effect of the metal contacts on detector bandwidth by depositing Al/Ti contacts on the Si<sub>2</sub>Te<sub>3</sub> flake. The output characteristics of the device showed a Schottky contact, see Fig. 6c. The devices exhibited lower photocurrent compare to the ones with Au/Cr metal contacts. However, they

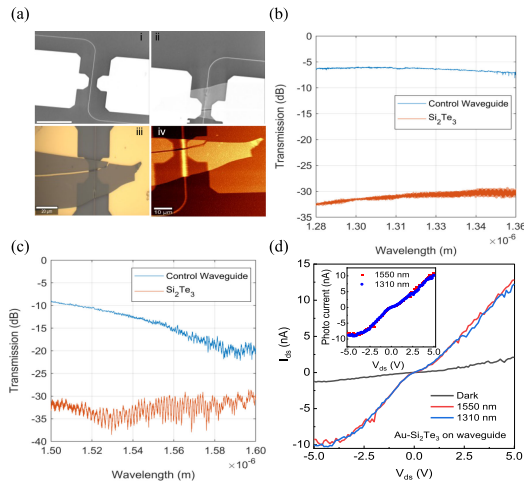


Fig. 7. Waveguide integrated Si<sub>2</sub>Te<sub>3</sub> photodetector. (a–(i-ii)) SEM image of the bare Si waveguide and waveguide with transferred Si<sub>2</sub>Te<sub>3</sub> flake. (a –(iii-iv)) Optical microscope and AFM images of waveguide covered by a multilayer exfoliated Si<sub>2</sub>Te<sub>3</sub> flake. (b) Transmission output of Si waveguide before and after the transfer of multilayer Si<sub>2</sub>Te<sub>3</sub> for 1310 nm laser propagation. (c) Transmission output of Si waveguide before and after the transfer of multilayer Si<sub>2</sub>Te<sub>3</sub> for 1550 nm laser propagation. (d) Output characteristics of the waveguide integrated Si<sub>2</sub>Te<sub>3</sub> photodetector under dark and telecom wavelengths respectively. Inset shows the generated photocurrent under the telecom wavelength excitations.

demonstrated a higher bandwidth of 3.8 MHz under the same bias and illumination conditions (See Fig. 6d).

### E. Si<sub>2</sub>Te<sub>3</sub> Integrated Si Waveguides

To check the potential of using Si<sub>2</sub>Te<sub>3</sub> for on-chip photodetectors, it is important to understand the feasibility of integrating the Si<sub>2</sub>Te<sub>3</sub> with a Si waveguide, and study the interaction of Si<sub>2</sub>Te<sub>3</sub> with the confined light. The Si photonic chips were fabricated using e-beam lithography and deep reactive ion etching at an external facility (Applied Nanotools Inc) and 100 nm gold metal pads were pre-deposited around the silicon structures. The SEM image of the bare Si waveguide is shown in Fig. 7a(i). The silicon waveguide has a cross section of height and width are 220 and 460 nm, respectively. Additionally, it has 2 μm buffered Si oxide (BOX). It is crucial to keep the measuring waveguide parameters unchanged before and after the transfer of the 2D materials to extract the losses due to the transferred material. The usual 2D dry transfer process yields unwanted flake transfer and contaminate the substrate surface with unwanted PDMS residues.

In this study, we utilized the deterministic 2D dry transfer process, which allows transferring the selected flake onto the target area with less contamination to the substrate and avoids the unwanted flake transfer. First, mechanically exfoliated Si<sub>2</sub>Te<sub>3</sub> flakes were transferred onto a PDMS substrate, that is used to align selected Si<sub>2</sub>Te<sub>3</sub> flake on to the pre-deposited Au electrodes placed on Si chip. Then, it is carefully transferred by selectively pushing the back side of the PDMS with a needle. Figure 7a(ii) shows a SEM image of the waveguide integrated Si<sub>2</sub>Te<sub>3</sub> photodetector. The optical and AFM images of the waveguide with flake were shown in Figs. 7a(iii-iv), respectively. The passive impact due to absorption or scattering of Si<sub>2</sub>Te<sub>3</sub> flake provides

TABLE I  
LOSSES ASSOCIATED WITH 2D MATERIALS / SI WAVEGUIDE HETEROGENEOUS PLATFORM

Material on Si waveguide	Thickness (nm)	Bandgap (eV)	Loss (dB/μm)	Ref
Graphene	monolayer	0	0.1 (1550)	[37]
Black Phosphorus	100	0.3	3.34 (1550 nm)	[16]
MoTe <sub>2</sub>	50	0.9	0.4 (1550 nm)	[38]
MoS <sub>2</sub>	50	1.3	0.037(1550 nm)	[39]
Si <sub>2</sub> Te <sub>3</sub>	90	Visible to NIR due to defects	0.69 (1550 nm) 0.86 (1310 nm)	This work

insights on the potential hybrid photodetector devices integration. Figures 7(b)-(c) show the corresponding propagation losses of a waveguide with Si<sub>2</sub>Te<sub>3</sub> a 90 nm thick flake at O-band and C-band wavelengths for the transverse magnetic (TM) mode. The observed high losses can be attributed to the absorption of Si<sub>2</sub>Te<sub>3</sub>, scattering of light out of the Si<sub>2</sub>Te<sub>3</sub> layer and optical mode mismatch between the bare and Si<sub>2</sub>Te<sub>3</sub> covered sections of the waveguide. However, based on the aforementioned photocurrent generation studies, we expect that the losses induced by absorption of the telecom wavelengths are also significant.

The wavelength dependence of the transmission in the C-band arises from a larger scattering out of the waveguide at circular bends (radius of 15 μm), which increases with the wavelength. From mode simulations, our waveguide (without accounting for side roughness) experiences bend losses of 0.034 dB/rad and 0.308 dB/rad at 1530 and 1570 nm respectively (this is equivalent to additional losses of 0.32 and 2.90 dB). In contrast, in the O-Band the induced bending losses are negligible. Micro ring resonators (MRR) were utilized on the same chip to calibrate the light polarization. A TM mode was coupled into the Si<sub>2</sub>Te<sub>3</sub>/Si waveguide. The measured additional losses arising from the Si<sub>2</sub>Te<sub>3</sub>/Si interface are  $18 \pm 2$  dB and  $24.3 \pm 2$  dB at 1550 nm and 1310 nm, respectively. This corresponds to 0.69 dB/μm and 0.86 dB/μm using a total interface length of 26 μm. Table I compares losses from different 2D materials/Si waveguide heterogeneous integration. The observed losses in the case of Si<sub>2</sub>Te<sub>3</sub> are lower than those induced by black phosphorus, but significantly larger than those induced by graphene and TMDC materials.

Finally, the waveguide integrated Si<sub>2</sub>Te<sub>3</sub> photodetector performance was evaluated. Figure 7d, demonstrates the output characteristics of the waveguide integrated Si<sub>2</sub>Te<sub>3</sub> photodetector with under 1550 nm (input power 0.57 mW for a coverage length of 26 μm) and 1310 nm (1.16 mW) wavelength excitations. The measured photocurrents are shown in the inset of Fig. 7d. The measured photo responsivities are 0.022 mA/W and 0.010 mA/W under 1550 nm and 1310 nm, respectively. These values are much lower than the responsivity values of Si<sub>2</sub>Te<sub>3</sub>

devices with top deposited metal contacts. This lower responsivity values can be attributed to the higher contacts resistance between the  $\text{Si}_2\text{Te}_3$  and the pre-deposited Au contacts of the fabricated chip. Moreover, the waveguide induced a strain effect on the  $\text{Si}_2\text{Te}_3$  electronic band structure. Therefore, optimizing the optical mode coupling of the waveguide with and without the 2D flake in addition to reducing the contact resistance between  $\text{Si}_2\text{Te}_3$  and the contact metals is essential in future waveguide integrated  $\text{Si}_2\text{Te}_3$  photodetector work.

### III. CONCLUSION

In summary, the photoconductive characteristics of a multilayered  $\text{Si}_2\text{Te}_3$  photodetector were investigated. The demonstrated responsivities are  $170.5 \text{ AW}^{-1}$  and  $12.1 \text{ AW}^{-1}$  under 1310 nm and 1550 nm telecom wavelength illuminations, respectively. Noteworthy, this is the first demonstration of such optoelectronic properties of  $\text{Si}_2\text{Te}_3$  in the mentioned bands. The devices exhibit a bandwidth of 1.6 MHz and 3.8 MHz with Au/Cr and Al/Ti contacts, respectively. Furthermore, we have demonstrated a heterogeneously integrated  $\text{Si}_2\text{Te}_3$  photodetector onto a silicon photonic waveguide. Although, the scope of this work is limited to understanding the telecom wavelengths interaction with  $\text{Si}_2\text{Te}_3$ , our preliminary results demonstrate the potential integration on Si photonic chips for application in optoelectronics.

### ACKNOWLEDGMENT

The authors are thankful to NYUAD Core Technology Platform Facility (CTP), and NYUAD Photonic Research Lab for the analytical, material characterization, device fabrication, and testing. The authors are also grateful to the research instrumentation specialist Mr. Nikolaos Giakoumidis from NYUAD CTP, for his help and support in the photonics lab.

### REFERENCES

- [1] D. Thomson *et al.*, "Roadmap on silicon photonics," *J. Opt.*, vol. 18, no. 7, 2016, Art. no. 073003, doi: [10.1088/2040-8978/18/7/073003](https://doi.org/10.1088/2040-8978/18/7/073003).
- [2] Y. Bolkhovityanov and O. Pchelyakov, "GaAs epitaxy on Si substrates: Modern status of research and engineering," *Phys.-Uspekhi*, vol. 51, 2008, Art. no. 437, doi: [10.1070/PU2008v051n05ABEH006529](https://doi.org/10.1070/PU2008v051n05ABEH006529).
- [3] N. Youngblood and M. Li, "Integration of 2D materials on a silicon photonics platform for optoelectronics applications," *Nanophotonics*, vol. 6, no. 6, pp. 1205–1218, 2017, doi: [10.1515/nanoph-2016-0155](https://doi.org/10.1515/nanoph-2016-0155).
- [4] W. Gebril, H. Salman, and M. O. Manasreh, "Near-Infrared photodetectors based on hybrid graphene-colloidal pbse quantum dots," *MRS Adv.*, vol. 5, no. 44, pp. 2273–2280, 2020, doi: [10.1557/adv.2020.256](https://doi.org/10.1557/adv.2020.256).
- [5] B. Dong, L. Huang, C. Lee, and K.-W. Ang, "Black phosphorus based photodetectors," in *Fundamentals and Applications of Phosphorus Nanomaterials*, vol. 1333, Washington, DC, USA: Amer. Chem. Soc., 2019, pp. 135–153.
- [6] Y. Wang *et al.*, "High-speed infrared two-dimensional platinum diselenide photodetectors," *Appl. Phys. Lett.*, vol. 116, no. 21, 2020, Art. no. 211101, doi: [10.1063/5.0010034](https://doi.org/10.1063/5.0010034).
- [7] T. Yu *et al.*, "Two-dimensional gep-based broad-band optical switches and photodetectors," *Adv. Opt. Mater.*, vol. 8, no. 2, 2020, Art. no. 1901490, doi: [10.1002/adom.201901490](https://doi.org/10.1002/adom.201901490).
- [8] G. Dushaq and M. Rasras, "Multilayer 2D germanium phosphide (GeP) infrared phototransistor," *Opt. Exp.*, vol. 29, no. 6, pp. 9419–9428, 2021, doi: [10.1364/OE.420431](https://doi.org/10.1364/OE.420431).
- [9] M. Amani *et al.*, "Solution-Synthesized high-mobility tellurium nanoflakes for short-wave infrared photodetectors," *ACS Nano*, vol. 12, no. 7, pp. 7253–7263, 2018, doi: [10.1021/acsnano.8b03424](https://doi.org/10.1021/acsnano.8b03424).
- [10] K. Zhang *et al.*, "Ultrasensitive near-infrared photodetectors based on a Graphene–mote2–Graphene vertical van der waals heterostructure," *ACS Appl. Mater. Interfaces*, vol. 9, no. 6, pp. 5392–5398, 2017, doi: [10.1021/acsnano.6b14483](https://doi.org/10.1021/acsnano.6b14483).
- [11] Z. Cheng *et al.*, "2D Materials enabled next-generation integrated optoelectronics: From fabrication to applications," *Adv. Sci.*, vol. 8, no. 11, 2021, Art. no. 2003834, doi: [10.1002/advs.202003834](https://doi.org/10.1002/advs.202003834).
- [12] J. Wu *et al.*, "Two-Dimensional materials for integrated photonics: Recent advances and future challenges," *Small Sci.*, vol. 1, no. 4, 2021, Art. no. 2000053, doi: [10.1002/ssmc.202000053](https://doi.org/10.1002/ssmc.202000053).
- [13] A. M. Askar, M. Saeed, A. Hamed, R. Negra, and M. M. Adachi, "Thickness-modulated lateral mos2 diodes with sub-terahertz cut-off frequency," *Nanoscale*, vol. 13, no. 19, pp. 8940–8947, 2021, doi: [10.1039/D1NR00089F](https://doi.org/10.1039/D1NR00089F).
- [14] Y. Ding *et al.*, "Ultra-compact integrated graphene plasmonic photodetector with bandwidth above 110 GHz," *Nanophotonics*, vol. 9, no. 2, pp. 317–325, 2020, doi: [10.1515/nanoph-2019-0167](https://doi.org/10.1515/nanoph-2019-0167).
- [15] V. Mišėikis *et al.*, "Ultrafast, zero-bias, graphene photodetectors with polymeric gate dielectric on passive photonic waveguides," *ACS Nano*, vol. 14, no. 9, pp. 11190–11204, 2020, doi: [10.1021/acsnano.0c02738](https://doi.org/10.1021/acsnano.0c02738).
- [16] N. Youngblood, C. Chen, S. J. Koester, and M. Li, "Waveguide-integrated black phosphorus photodetector with high responsivity and low dark current," *Nat. Photon.*, vol. 9, no. 4, pp. 247–252, 2015, doi: [10.1038/nphoton.2015.23](https://doi.org/10.1038/nphoton.2015.23).
- [17] R. Maiti *et al.*, "Strain-engineered high-responsivity mote2 photodetector for silicon photonic integrated circuits," *Nat. Photon.*, vol. 14, no. 9, pp. 578–584, 2020, doi: [10.1038/s41566-020-0647-4](https://doi.org/10.1038/s41566-020-0647-4).
- [18] C. Lan, Z. Shi, R. Cao, C. Li, and H. Zhang, "2D materials beyond graphene toward Si integrated infrared optoelectronic devices," *Nanoscale*, vol. 12, no. 22, pp. 11784–11807, 2020, doi: [10.1039/D0NR02574G](https://doi.org/10.1039/D0NR02574G).
- [19] A. T. Hoang, K. Qu, X. Chen, and J.-H. Ahn, "Large-area synthesis of transition metal dichalcogenides via CVD and solution-based approaches and their device applications," *Nanoscale*, vol. 13, pp. 615–633, 2021, doi: [10.1039/D0NR08071C](https://doi.org/10.1039/D0NR08071C).
- [20] X. Song *et al.*, "Synthesis of large-area uniform  $\text{Si}_2\text{Te}_3$  thin films for p-type electronic devices," *Nanoscale*, vol. 12, no. 20, pp. 11242–11250, 2020, doi: [10.1039/D0NR01730B](https://doi.org/10.1039/D0NR01730B).
- [21] S. Keuleyan, M. Wang, F. R. Chung, J. Commons, and K. J. Koski, "A silicon-based two-dimensional chalcogenide: Growth of  $\text{Si}_2\text{Te}_3$  nanoribbons and nanoplates," *Nano Lett.*, vol. 15, no. 4, pp. 2285–2290, 2015, doi: [10.1021/nl504330g](https://doi.org/10.1021/nl504330g).
- [22] D. Bletskan, "Electronic structure, optical and photoelectrical properties of crystalline  $\text{Si}_2\text{Te}_3$ ," *Semicond. Phys., Quantum Electron. Optoelectron.*, vol. 22, pp. 267–276, 2019, doi: [10.15407/spqeo22.03.267](https://doi.org/10.15407/spqeo22.03.267).
- [23] X. Shen, Y. S. Puzyrev, C. Combs, and S. T. Pantelides, "Variability of structural and electronic properties of bulk and monolayer  $\text{Si}_2\text{Te}_3$ ," *Appl. Phys. Lett.*, vol. 109, no. 11, 2016, Art. no. 113104, doi: [10.1063/1.4962826](https://doi.org/10.1063/1.4962826).
- [24] K. Wu *et al.*, "Structure and photoluminescence study of silicon based two-dimensional  $\text{Si}_2\text{Te}_3$  nanostructures," *J. Appl. Phys.*, vol. 122, no. 7, 2017, Art. no. 075701, doi: [10.1063/1.4998811](https://doi.org/10.1063/1.4998811).
- [25] M. Wang, G. Lahti, D. Williams, and K. J. Koski, "Chemically tunable full spectrum optical properties of 2D silicon telluride nanoplates," *ACS Nano*, vol. 12, no. 6, pp. 6163–6169, 2018, doi: [10.1021/acsnano.8b02789](https://doi.org/10.1021/acsnano.8b02789).
- [26] J. Kwak, K. Thiyagarajan, A. Giri, and U. Jeong, "Au-Assisted catalytic growth of  $\text{Si}_2\text{Te}_3$  plates," *J. Mater. Chem. C*, vol. 7, no. 34, pp. 10561–10566, 2019, doi: [10.1039/C9TC03769A](https://doi.org/10.1039/C9TC03769A).
- [27] K. Wu and J. Cui, "Morphology control of  $\text{Si}_2\text{Te}_3$  nanostructures synthesized by CVD," *J. Mater. Sci.: Mater. Electron.*, vol. 29, pp. 15643–15648, 2018, doi: [10.1007/s10854-018-9158-1](https://doi.org/10.1007/s10854-018-9158-1).
- [28] J. Chen *et al.*, "2D Silicon-based semiconductor  $\text{Si}_2\text{Te}_3$  toward broad-band photodetection," *Small*, vol. 17, no. 13, 2021, Art. no. 2006496, doi: [10.1002/smll.202006496](https://doi.org/10.1002/smll.202006496).
- [29] K. C. Göbgen, S. Steinberg, and R. Dronskowski, "Revisiting the Si-Te system: Site2 finally found by means of experimental and quantum-chemical techniques," *Inorganic Chem.*, vol. 56, no. 18, pp. 11398–11405, 2017, doi: [10.1021/acs.inorgchem.7b01847](https://doi.org/10.1021/acs.inorgchem.7b01847).
- [30] K. Ploog, W. Stetter, A. Nowitzki, and E. Schönherr, "Crystal growth and structure determination of silicon telluride  $\text{Si}_2\text{Te}_3$ ," *Mater. Res. Bull.*, vol. 11, no. 9, pp. 1147–1153, 1976, doi: [10.1016/0025-5408\(76\)90014-3](https://doi.org/10.1016/0025-5408(76)90014-3).
- [31] J. Chen, R. Bhattarai, J. Cui, X. Shen, and T. Hoang, "Anisotropic optical properties of single  $\text{Si}_2\text{Te}_3$  nanoplates," *Sci. Rep.*, vol. 10, no. 1, 2020, Art. no. 19205, doi: [10.1038/s41598-020-76265-1](https://doi.org/10.1038/s41598-020-76265-1).

- [32] K. Ziegler and U. Birkholz, "Photoelectric properties of Si<sub>2</sub>Te<sub>3</sub> single crystals," *Physica Status Solidi*, vol. 39, no. 2, pp. 467–475, 1977, doi: [10.1002/pssa.2210390213](https://doi.org/10.1002/pssa.2210390213).
- [33] J. Chen *et al.*, "2D Silicon-based semiconductor Si<sub>2</sub>Te<sub>3</sub> toward broadband photodetection," *Small*, vol. 17, no. 13, 2021, Art. no. 2006496, doi: [10.1002/sml.202006496](https://doi.org/10.1002/sml.202006496).
- [34] Z. Yin *et al.*, "Single-Layer MoS<sub>2</sub> phototransistors," *ACS Nano*, vol. 6, no. 1, pp. 74–80, 2012, doi: [10.1021/nm2024557](https://doi.org/10.1021/nm2024557).
- [35] S. R. Tamalampudi *et al.*, "High performance and bendable few-layered in-se photodetectors with broad spectral response," *Nano Lett.*, vol. 14, no. 5, pp. 2800–2806, 2014, doi: [10.1021/nl500817g](https://doi.org/10.1021/nl500817g).
- [36] J. M. An, A. Franceschetti, and A. Zunger, "Pauli blocking versus electrostatic attenuation of optical transition intensities in charged pbse quantum dots," *Phys. Rev. B*, vol. 76, no. 16, 2007, Art. no. 161310, doi: [10.1103/PhysRevB.76.161310](https://doi.org/10.1103/PhysRevB.76.161310).
- [37] Y. Ding *et al.*, "Effective electro-optical modulation with high extinction ratio by a graphene–silicon microring resonator," *Nano Lett.*, vol. 15, no. 7, pp. 4393–4400, 2015, doi: [10.1021/acs.nanolett.5b00630](https://doi.org/10.1021/acs.nanolett.5b00630).
- [38] R. Maiti *et al.*, "A semi-empirical integrated microring cavity approach for 2D material optical index identification at 1.55 μm," *Nanophotonics*, vol. 8, no. 3, pp. 435–441, 2019, doi: [10.1515/nanoph-2018-0197](https://doi.org/10.1515/nanoph-2018-0197).
- [39] R. Maiti *et al.*, "Loss and coupling tuning via heterogeneous integration of mos2 layers in silicon photonics [Invited]," *Opt. Mater. Exp.*, vol. 9, no. 2, pp. 751–759, 2019, doi: [10.1364/OME.9.000751](https://doi.org/10.1364/OME.9.000751).



**Juan E. Villegas** (Student Member, IEEE) received the M.Sc. degree in microsystems engineering from Masdar Institute, Khalifa University, Abu Dhabi, UAE. He is currently working toward the Ph.D. degree with the New York University of Abu Dhabi, Abu Dhabi, UAE. He has worked in the fabrication of Silicon Photonic devices and in the development of materials for photonic applications, using low temperature a-Si, oxides, and polymers. His work is focused on the study of plasmonic and its usage in cyber security applications.



**Bruna Paredes** received the master's degree in electronics and telecommunications engineering from the University of Aveiro, Portugal, in 2014. She is currently a Research Engineer with the New York University of Abu Dhabi, Abu Dhabi, UAE. Her research interests include designing and testing optical devices within photonics integrated circuits.



**Srinivasa R. Tamalampudi** received the M.S. degree in microsystems engineering from Hochschule Furtwangen, Germany, in 2009, and the Ph.D. degree in physics from Academia Sinica, Taiwan International Graduate Program (TIGP), Taiwan, in 2015. From 2016 to 2017, he was a Research Associate with the University of Cambridge, Cambridge, U.K. From 2017 to 2020, he was a Postdoctoral Fellow with the Khalifa University of Science and Technology, Abu Dhabi, UAE. He is currently a Research Associate with the New York University of Abu Dhabi, Abu

Dhabi, UAE. His current research interests include heterogeneous integration of 2D materials onto Si photonic chips for optoelectronic applications, such as photo-detectors, modulators and light emitting devices.



**Ghada Dushaq** received the bachelor's degree (with distinction) in physics and mathematics from BirZeit University, Palestine, in 2009. She went on to graduate with the M.Sc. degree in physics from the University of Jordan, Amman, Jordan, in 2012, funded by German Academic Exchange Service (DAAD), followed by the Ph.D. degree in microsystems engineering from the Masdar Institute of Science and Technology (Khalifa University), Abu Dhabi, UAE, under a Cooperative Program with the Massachusetts Institute of Technology, Cambridge, MA, USA. She

graduated with her doctorate in 2017. She is currently a Research Associate with the New York University of Abu Dhabi, Abu Dhabi, UAE. Her research work in applied physics investigates new and innovative materials, structures, and process technologies in order to improve the performance of high-speed optoelectronics, nanoelectronics, and photonics devices. Her research on the use of silicon, germanium, III-V compound semiconductors, and two-dimensional materials can improve the efficiency and address limitations of currently available technologies.



**Mahmoud S. Rasras** (Senior Member, IEEE) received the Ph.D. degree in physics from the Catholic University of Leuven, Belgium, in 2000. He is currently an Associate Professor of electrical and computer engineering with New York University, Abu Dhabi, UAE. His Ph.D. research was pursued with IMEC (Interuniversity Microelectronics Center) focused on the development of a spectroscopic photon-emission microscopy technique to study CMOS device reliability. His group at NYUAD is working on a variety of research problems to address the current

limitation of communication bandwidth. His research targets the design of high-speed transceiver circuits for 400Gb/s links in addition to developing process technology for low-temperature germanium photodetectors integration on CMOS compatible platform (above 64 Gb/s). Currently, much of his group research efforts is focused on the integration of 2D materials on Silicon photonics platform for on-chip optical interconnect and sensing applications.